Molecule stapling-assisted fabrication of high-quality $CsPbI_2Br$ films for efficient and stable photovoltaic modules

Ruihao Chen (rhchen@nwpu.edu.cn)
Northwestern Polytechnical University https://orcid.org/0000-0001-8425-1234
Jieru Du
Northwestern Polytechnical University
Xuan Zheng
Minnan Normal University
Feiming Li
Minnan Normal University
Pengfei Guo
Northwestern Polytechnical University
Zhe Liu
Northwestern Polytechnical University
Hongqiang Wang (hongqiang.wang@nwpu.edu.cn)
Northwestern Polytechnical University

Research Article

Keywords: Molecule stapling, CsPbI2Br solar cells, large-area module

Posted Date: October 12th, 2022

DOI: https://doi.org/10.21203/rs.3.rs-2149037/v2

Abstract

$CsPbI_2Br$ perovskite solar cells (PSCs) are a suitable bandgap for the fabrication of tandem solar cells and have excellent thermal stability. However, their halide phase separation and water instability lead to challenges for practical industrialization. Here, a molecular stapling strategy is demonstrated to assist in the fabrication/stabilization of a high-quality large-area $CsPbI_2Br$ film by using a series of cesium perfluorodioate salts. According to density functional theory and experimental attempts, hexafluoroglutarate anions possessed a stronger interaction between chelated oxyen and surface Pb^{2+} ions due to the matchable stapling configuration, which effectively improved moisture tolerance, reduced defects and further improved the phase stability of the $CsPbI_2Br$ films. In the prepared high-quality $CsPbI_2Br$ films, the fabricated PSCs achieved 16.4% efficiency in a small area. The devices displayed high stability, retaining ~91% of the initial efficiency for more than 1000 h under 85 °C and N_2 conditions and ~90% for 2000 h at a relative humidity of 20% without encapsulation. More importantly, this developed strategy can be employed for the production of large-area perovskite solar modules. A mini perovskite solar module with an efficiency up to 12.4% in a large area of 16 cm^2 was successfully fabricated.

Introduction

With the rapid development in the successful production of metal-halide hybrid perovskite films and device configuration upgrades,[1, 2] perovskite solar cells (PSCs) have become a prospective candidate for next-generation low-cost and high-efficiency photovoltaics.[3] However, the instability of organic–inorganic hybrid PSCs still remains unsolved due to the volatility of their organic components (especially $CH_3NH_3^+$ organic component), which often cause degradation of devices under either air or thermal conditions.[4-9] Replacing the organic cations with inorganic cesium ions (Cs^+) can offer an inherently thermally stable perovskite phase over 400 °C with a tunable bandgap between 1.73 eV for $CsPbI_3$ and 2.25 eV for $CsPbBr_3$ by different halides.[10, 11] Among the above inorganic perovskites, $CsPbI_2Br$ perovskite[12-14] is considered to be a good candidate for high-performance and robust all-inorganic devices due to its reasonable Goldschmidt tolerance factor and suitable band gap. Currently, the power conversion efficiency (PCE) of $CsPbI_2Br$ devices is over 16%[15-17], but fabricating scalable, uniform and dense $CsPbI_2Br$ films and stabilizing them under moisture and light illumination are the main challenges for the improvement of the PV performance of corresponding devices and their practicability.

Unfortunately, similar to the moisture instability of the black-phase $CsPbI_2Br$ structure, the $CsPbI_2Br$ polycrystalline film easily transforms into a nonphotoactive phase during the production procedure and reduces the corresponding PSC performance, especially under ambient air conditions. Various strategies to tackle this problem, such as crystallization regulation,[18, 19] interface/surface engineering,[20-23] and mixed heterojunction structures,[24,25] have been employed to fabricate high-quality $CsPbI_2Br$ films for high-performance PSCs. For example, Lewis bases, such as amino-functionalized polymers (PN4N)[26] and polyvinyl pyrrolidone (PVP)[27] as interlayers, have been

employed to not only improve the crystallinity of $CsPbI_2Br$ films but also interact strongly with Pb^{2+} ions from $CsPbI_2Br$ films to surface trap states. As novel Lewis bases, oxoacid salts[28-31] have been reported as dopants that can regulate film growth and enhance the overall stability by the merit of strong Pb-O bonds interacting with uncoordinated Pb^{2+} ions. For example, lead (II) propionate[32] used as an additive in the $CsPbI_2Br$ precursor certainly improved PSC environmental stability and showed a higher PCE of 14.58%, attributed to improved crystallinity and photoluminescence and defect passivation. In principle, a reliable and effective additive agent for perovskites can be achieved by tailoring the uniform $CsPbI_2Br$ film growth and inhibiting water attack during the crystallization process. Among various bonding types, stapling coordination has a special bonding mode of polydentate molecules to metal ions and enhances the bonding ability compared to that of conventional monodentate additives. However, there is still a lack of a rational structure design method for effective perovskite coordination. Therefore, exploiting a facile strategy to produce and stabilize high-quality and robust inorganic $CsPbI_2Br$ films represents a tough challenge for highly efficient and ultrastable inorganic PSCs toward potential large-scale fabrication.

Here, we report new additive engineering to use a series of cesium perfluorodioate salts as effective dopants for inducing high-quality perovskite film crystallization and blocking water invasion, thus promoting the stabilization of highly stable $CsPbI_2Br$ films for photovoltaics. According to density functional theory and experimental trials, cesium hexafluoroglutarate (i.e., $C_5F_6O_4Cs_2$) was optimized and used to assist the formation of even and high-quality $CsPbI_2Br$ films and enrichingly stapled in grain boundaries and interfaces to coordinate the unsaturated Pb^{2+} ions. Multifluorine atoms can resist moisture attack and fix halide ions to suppress I/Br halide phase segregation. Consequently, together with excellent long-term moisture and thermal stabilities, the $C_5F_6O_4Cs_2$-based PSCs achieved a champion efficiency of 16.4%. Moreover, 16-cm^2-area PSC modules based on molecular-stapling $CsPbI_2Br$ films were successfully constructed and had the best efficiency of over 12.4% by blade coating.

Results And Discussion

Molecule stapling-assisted growth of high-quality $CsPbI_2Br$ films

In this work, a stapling binding additive, cesium hexafluoroglutarate (i.e., $C_5F_6O_4Cs_2$), was added to the fabrication procedure of $CsPbI_2Br$ perovskite films *via* typical coating methods (such as spin coating or blade coating). $C_5F_6O_4Cs_2$ was produced by the reaction of hexafluoroglutaric acid with Cs_2CO_3 and further purification. In particular, the optimized amount of $C_5F_6O_4Cs_2$ powder was mixed into the $CsPbI_2Br$ solution and then involved in the production of $CsPbI_2Br$ films by solvent evaporation, as shown in the Supporting Information (SI). As proposed in Figure 1a, due to the strong chelation of $C_5F_6O_4Cs_2$ with Pb^{2+} ions[33, 34,] $C_5F_6O_4Cs_2$ was introduced into the perovskite precursor to regulate the growth of perovskite films by retarding film crystallization. As shown in Figure 1b, c and S1, the $C_5F_6O_4Cs_2$-stapled $CsPbI_2Br$ film (denoted as Cs-HFG) showed a dense and more even surface

morphology than the control film. The F and O element mapping of EDS analysis confirmed the uniform distribution of $C_5F_6O_4^{2-}$ ions on the perovskite film's bulk phase and surface (Figure S1-2). As seen in the XRD patterns, the intensities of the [100] and [200] oriented peaks of the Cs-HFG film were obviously increased compared to those of the control sample. PL and UV—vis spectra (Figure 1d-f) indicated that $C_5F_6O_4Cs_2$ stapling effectively improved the crystallinity and quality of $CsPbI_2Br$ films, indicating largely decreased nonradiative recombination defects. Based on the XRD patterns and PL and UV—vis spectra, the $C_5F_6O_4Cs_2$ doping content was optimized to be 1.5 mg/mL for the precursor solution during film fabrication (Figure S3-5).

To verify the rationality of the stapling molecule design, we designed and synthesized a series of cesium perfluorodioates, including cesium tetrafluorosuccinate ($C_4F_4O_4Cs_2$, TFS), cesium hexafluoroglutarate ($C_5F_6O_4Cs_2$, HFG) and cesium octafluorohexanedioate ($C_6F_8O_4Cs_2$, OFA), to introduce into the perovskite films by the same process as for Cs-HFG films. As seen in Figure S6, the decomposition temperatures of all cesium perfluorodioates exceed 200 °C, indicating excellent thermal stability. We used density functional theory (DFT) to calculate the adsorption energies (DE_{ad}) of perfluorodioate anions onto the perovskite surface. For simplification, the α-phase $CsPbI_3$ structure was used as a paradigm, and the computational details are also given in SI. As shown in Figures 1g and S7 and Table S1, the results show that HFG can be adsorbed strongly on the perovskite surface with a maximum adsorption energy (-8.76 eV), while TFS and OFA on the surface possess weaker absorption energies (-7.15 eV and -5.96 eV, respectively). In addition, the optimized structures of these perfluorodioate salts show that the molecular radial length of HFG is 6.28 Å, which is basically matched with that of Br-Pb-Br (6.0 Å)[35] to I-Pb-I (6.2 Å)[36]. the edge length of the $CsPbI_2Br$ cell, while those of TFS and OFA are 5.11 Å and 7.73 Å, respectively. Combined with the above results, these results suggest that size matching before absorption may also be an important reason for the stability enhancement of the $CsPbI_2Br$ film with HFG. As shown in Figures S8–9, all cesium perfluorodioates could evidently ameliorate the film quality and PL intensity of the $CsPbI_2Br$ films when compared with the control film. These results underlined the fact that dicarboxylate anions are ideal candidates for crystallization and defect passivation in perovskites.

Molecule stapling improved $CsPbI_2Br$-based photovoltaic performance

Benefiting from the improvement, we used the configuration of ITO/SnO_2/$CsPbI_2Br$/Spiro-OMeTAD/Au to fabricate the regular PSCs (Figure S10). A high PCE of 16.43% in the RS mode with a high V_{oc} of 1.30 V, a high FF of 74.83% and J_{sc} of 16.89 mA·cm^{-2} were readily obtained in the Cs-HFG cells, which obviously exceeded that of the best-performance control sample possessing an efficiency of RS 11.36% with a lower FF of 62.93%, J_{sc} of 15.17 mA·cm^{-2} and V_{oc} of 1.19 V under AM 1.5 G illumination, as shown in Figure 2a. For the FS mode, a much higher efficiency of 16.31% was realized in the Cs-HFG device than 9.77% in the control device. Integrated currents sourced from the incident photon-to-electron conversion efficiency (IPCE) spectrum data were 15.93 and 13.99 mA·cm^{-2} for Cs-HFG and control devices,

respectively, which are in accord with their results of *J-V* measurements (mismatch by approximately 2.4%) (Figure 2b). Moreover, the Cs-HFG devices presented average PCEs of RS 15.87% and FS 15.63% with a narrower distribution in comparison with control PSCs (RS 10.45% and 9.01%) (Table S2), indicating the superior repeatability of the Cs-HFG devices (Figure 2c). As shown in Figures S11 and Table S3, the efficiencies of all devices with different $C_5F_6O_4Cs_2$ concentrations were promoted compared with the control sample. The optimized amount of $C_5F_6O_4Cs_2$ for additive engineering was demonstrated to be 1.5 mg/mL, which is consistent with the above PL and XRD analysis results. Moreover, the PSCs treated with TFS (RS 15.07%) or OFA (RS 15.19%) salts also displayed improved PV performance (Figures S12 and Table S4). Here, the stabilized operating PCE of the Cs-HFG device was examined to be 16.28% at the maximum power point (MPP) tracking for approximately 400 s (Figure 2d), proving the better performance than that of the control device (10.80%). Under 25 °C and 30% RH storage conditions (Figure 2e), the unencapsulated Cs-HFG devices had a significant increase in stability and maintained 91.0% of the original efficiency after 300 h, while the control sample dropped to 33.0% of its original value, which should have been attributed to the hydrophobicity of the multifluoride atoms from the $C_5F_6O_4^{2-}$ ion and further confirmed by the water contact angle of 57.8° increasing from 40.2° in the control film (Figure S13). Meanwhile, as seen in Figure 2f, the Cs-HFG PSCs showed markedly improved light stability and maintained 91.8% of the original PCE, while control devices rapidly dropped to 36% of their original efficiency after 500 h under AM 1.5G illumination in a N_2 atmosphere. These results suggested that $C_5F_6O_4^{2-}$ stapling effectively improved the performance of $CsPbI_2Br$-based PSCs.

Reducing $CsPbI_2Br$ defects by strong interaction between $C_5F_6O_4^{2-}$ and $CsPbI_2Br$

To further study the regulatory mechanisms of molecular stapling, X-ray photoelectron spectroscopy (XPS) measurements were used to examine the detailed chemical states in the Cs-HFG films. Compared to the control film, the binding energies of the Pb $4f_{7/2}$ and Pb $4f_{5/2}$ peaks for the Cs-HFG film increased (Figure S14). The peaks of C 1 s, F 1 s, and O 1 s in the Cs-HFG film confirm the existence of the $C_5F_6O_4^{2-}$ ion and the new chemical bond of Pb–O on the perovskite film (Figures 3a and S15). We concluded that $C_5F_6O_4^{2-}$ could not be doped into the perovskite lattice but reorganized on the perovskite surface and boundaries by strongly interacting with Pb^{2+} ions. To further elucidate the stapling interaction of $C_5F_6O_4^{2-}$ with the perovskite films, we used Raman spectroscopy to detect the Pb-O bond (Figure 3b). The feature peak of perovskite is broad at approximately 100 cm^{-1}. Interestingly, a new peak at 149 cm^{-1} emerged, which can be ascribed to the Pb–O bond that was derived from the $C_5F_6O_4^{2-}$ interacting with the Pb^{2+} ion, consistent with previous research work[37].

To reflect the surface valence band level, the XPS valence band spectra were studied, as shown in Figure 3c. The maximum valence band (VBM) of the Cs-HFG film is 1.05 eV and is higher than that of the control sample (0.95 eV), which would promote an increase in V_{oc} for the Cs-HFG device. As seen in Figure 3d, the built-in potentials (V_{bi}) in both cells are also assessed by Mott–Schottky analysis, which plots C^{-2} versus V. The extracted V_{bi} increased from 1.05 V in the control sample to 1.17 V in the Cs-HFG cell. The

ΔV_{bi} of 120 mV should help increase the V_{oc} and FF of the Cs-HFG cells. As characterized by the time-resolved PL spectra (Figure S16), the longer decay time of 360 ns in the Cs-HFG film than that of 140 ns in the control film revealed that the nonradiative recombination was effectively decreased by molecular stapling. The leakage current was significantly reduced in the Cs-HFG device under dark circumstances (Figure 3e). The Nyquist plots for the PSCs based on control and Cs-HFG films were measured at 0 V bias under dark conditions. The recombination resistance R_{rec} derived from the low frequency region increased from 1.14×10^4 to 2.06×10^5 Ω after $C_5F_6O_4^{2-}$ passivation (Figure 3f). The lower transfer resistance and higher recombination resistance in the Cs-HFG cell also confirmed the better carrier extraction and less nonradiative recombination. The above results demonstrated that molecule stapling not only reduced the trap state density of $CsPbI_2Br$ films but also accelerated interfacial charge transfer, which was beneficial for scalable and reproducible fabrication of modules. Compared to the control film, the FTIR spectra of the Cs-HFG film obviously showed three peaks belonging to the $-COO^-$ and $-CF_2-$ groups, which further confirmed the presence of $C_5F_6O_4^{2-}$ ions in the solid $CsPbI_2Br$ films (Figure S17).

Moreover, in accelerated moisture-aging experiments (20 °C and RH 70%), the Cs-HFG film still retained the black phase of perovskite, in contrast with the colorless phase of the control film over 4 min, which indicated that $C_5F_6O_4^{2-}$ effectively stabilized the $CsPbI_2Br$ film (Figure S18). As shown in Figure S19, the intensities of the (100) and (200) XRD peaks of black-phase $CsPbI_2Br$ became slightly weakened in the Cs-HFG film, and only a small amount of the d phase emerged, in contrast to the black phase in the control film, which mostly degraded to the d phase for over 3 min, which was consistent with the above results of device moisture stability. Halide phase separation has been certified to be a possible origin of $CsPbI_2Br$ cell intrinsic degradation in continuous operation, which can be detected by PL spectra under AM 1.5G illumination. As seen in Figure S20, the PL peak of the control film had a redshift of approximately 9 nm, while in the Cs-HFG film, the PL peak had no obvious change under continuous light illumination for 50 min, suggesting that $C_5F_6O_4^{2-}$ effectively suppressed I^- or Br^- migration in halide separation to promote performance enhancement. Encouraged by the robust stability of the Cs-HFG film, we further used P3HT as an HTL to test the thermal stability of $CsPbI_2Br$ devices, and the increased PCE of the target device was 14.57% compared to the 9.38% PCE of the control device (Figure 4b and Table S5). Under 85 °C and N_2 atmosphere, the Cs-HFG device retained 92.9% of its original value, while the control device rapidly dropped to 65.0% of its initial value for 400 h (Figure 4b). Based on the above results, such an improvement will be helpful to enhance the stability of $CsPbI_2Br$ films in PSC modules.

Large-area modules based on Cs-HFG films by blade coating

In addition to the photovoltaic performance, another issue for the future commercialization of PSCs is their large-scale modules. With this motivation, the stapling engineering developed in this work was extended to fabricate large-area perovskite films and then fabricate inorganic PSC modules in the configuration $FTO/SnO_2/CsPbI_2Br/Spiro\text{-}OMeTAD/Au$[38]. A schematic illustration of

the fabrication process by blade coating and post annealing is shown in Figure S21. The mini module has four subcells and an overall size of 4 × 4 cm^2 (16 cm^2) (Figure 4c, d), and the optimized laser-patterning lines were described in previous works[39, 40]. As shown in Figure 4e, the 8-cm^2-active-area Cs-HFG module exhibited a J_{sc} of 3.81 $mA{\cdot}cm^{-2}$, V_{oc} of 4.49 V, and a high FF of 72.01%, giving a PCE of RS 12.35%, which is one of the highest PCEs among the reported inorganic Cs-based PSC modules by blade or spin coating methods (Table S6). In the FS scan, an efficiency of 12.07% with a J_{sc} of 3.76 $mA{\cdot}cm^{-2}$, V_{oc} of 4.52 V, and an FF of 71.03% was achieved (Table S7). Moreover, the excellent reproducibility in the (RS 11.7±0.5%, FS 11.4±0.6%) efficiencies of 15 modules was verified (Figure 4f). This stapling passivation strategy shows the great potential of this additive engineering for the production of stable and large-area all-inorganic perovskite solar modules.

Conclusions

In summary, a molecular stapling strategy of stapling additives for $CsPbI_2Br$ polycrystalline films was proposed and successfully implemented by assisting the fabrication of high-quality $CsPbI_2Br$ films using cesium perfluorodioate salts. It was experimentally and theoretically demonstrated that due to the strong stapling interaction between dicarbonate and Pb^{2+} ions, moisture invasion was effectively inhibited by fluorine groups, thus improving phase stability and suppressing halide segregation in $CsPbI_2Br$ films. Consequently, equipped with cesium hexafluoroglutarate, the corresponding devices favorably achieved the champion efficiency of 16.4% with less hysteresis. Moreover, blade-coated large-area PSC modules based on molecular-stapling $CsPbI_2Br$ films were successfully produced and had a champion efficiency over 12.4% on 16 cm^2 of total area with high reproducibility. This stapling binding strategy for additive engineering of scalable inorganic perovskite films will help promote the commercialization of stable perovskite modules.

Declarations

Conflicts of interest

There are no conflicts to declare.

Acknowledgments

This work was financially supported by the Fundamental Research Funds for the Central Universities (G2022KY05106) and Xi’an Association for Science and Technology (095920221377).

References

1 Z. Gong, W. Zheng, Y. Gao, P. Huang, D. Tu, R. Li, J. Wei, W. Zhang, Y. Zhang and X. Chen, *Angew Chem Int Ed Engl*, 2019, **58**, 6943-6947.

2 Z. Li, C. Liu, X. Zhang, G. Ren, W. Han and W. Guo, *Small*, 2019, **15**, e1804692.

3 https://www.nrel.gov/pv/cell-efficiency.html.

4 Y. Guo, O. Yaffe, T. D. Hull, J. S. Owen, D. R. Reichman and L. E. Brus, *Nat. Commun.*, 2019, **10**, 1175.

5 H. Wang, X. Zhang, Q. Wu, F. Cao, D. Yang, Y. Shang, Z. Ning, W. Zhang, W. Zheng, Y. Yan, S. V. Kershaw, L. Zhang, A. L. Rogach and X. Yang, *Nat. Commun.*, 2019, **10**, 665.

6 Z. Wang, Z. Shi, T. Li, Y. Chen and W. Huang, *Angew. Chem. Int. Ed.*, 2017, **56**, 1190-1212.

7 M. Saliba, J.-P. Correa-Baena, M. Grätzel, A. Hagfeldt and A. Abate, *Angew. Chem. Int. Ed.*, 2018, **57**, 2554-2569.

8 S. Ippili, V. Jella, J.-H. Eom, J. Kim, S. Hong, J.-S. Choi, V.-D. Tran, N. Van Hieu, Y.-J. Kim, H.-J. Kim and S.-G. Yoon, *Nano Energy*, 2019, **57**, 911-923.

9 Y. Rong, Y. Hu, A. Mei, H. Tan, M. I. Saidaminov, S. I. Seok, M. D. McGehee, E. H. Sargent and H. Han, *Science*, 2018, **361**, eaat8235.

10 J. He, J. Liu, Y. Hou, Y. Wang, S. Yang and H. G. Yang, *Nat. Commun.*, 2020, **11**, 4237.

11 J. Duan, T. Hu, Y. Zhao, B. He and Q. Tang, *Angew. Chem. Int. Ed.*, 2018, **130**, 5848-5851.

12 C. Liu, Y. Yang, C. Zhang, S. Wu, L. Wei, F. Guo, G. M. Arumugam, J. Hu, X. Liu, J. Lin, R. E. I. Schropp and Y. Mai, *Adv. Mater.*, 2020, **32**, e1907361.

13 X. Gong, L. Guan, Q. Li, Y. Li, T. Zhang, H. Pan, Q. Sun, Y. Shen, C. Gratzel, S. M. Zakeeruddin, M. Gratzel and M. Wang, *Sci. Adv.*, 2020, **6**, eaay5661.

14 J. Zhang, W. Zhao, S. Olthof and S. F. Liu, *Small Methods*, 2021, **5**, e2100725.

15 Q. Tai, K.-C. Tang and F. Yan, *Energy Environ. Sci.*, 2019, **12**, 2375-2405.

16 J. Duan, H. Xu, W. E. I. Sha, Y. Zhao, Y. Wang, X. Yang and Q. Tang, *J. Mater. Chem. A*, 2019, **7**, 21036-21068.

17 Y. Y. Zhou and Y. X. Zhao, *Energy Environ. Sci.*, 2019, **12**, 1495-1511.

18 P. Wang, X. Zhang, Y. Zhou, Q. Jiang, Q. Ye, Z. Chu, X. Li, X. Yang, Z. Yin and J. You, *Nat. Commun.*, 2018, **9**, 2225.

19 W. Chen, H. Chen, G. Xu, R. Xue, S. Wang, Y. Li and Y. Li, *Joule*, 2019, **3**, 191-204.

20 J. Liang, Z. Liu, L. Qiu, Z. Hawash, L. Meng, Z. Wu, Y. Jiang, K. Ono Luis and Y. Qi, *Adv. Energy Mater.*, 2018, **8**, 1800504.

21 M. H. Li, J. Y. Shao, Y. Jiang, F. Z. Qiu, S. Wang, J. Zhang, G. Han, J. Tang, F. Wang, Z. Wei, Y. Yi, Y. W. Zhong and J. S. Hu, *Angew. Chem. Int. Ed.*, 2021, **60**, 16388-16393.

22 A. Wang, X. Deng, J. Wang, S. Wang, X. Niu, F. Hao and L. Ding, *Nano Energy*, 2021, **81**, 105631.

23 Y. Zhang, C. Wu, D. Wang, Z. Zhang, X. Qi, N. Zhu, G. Liu, X. Li, H. Hu, Z. Chen, L. Xiao and B. Qu, *Solar RRL*, 2019, **3**, 1900254.

24 J. Zhang, D. Bai, Z. Jin, H. Bian, K. Wang, J. Sun, Q. Wang and S. Liu, *Adv. Energy Mater.*, 2018, **8**, 1703246.

25 S. Yang, W. Liu, Y. Han, Z. Liu, W. Zhao, C. Duan, Y. Che, H. Gu, Y. Li and S. Liu, *Adv. Energy Mater.*, 2020, **10**, 2002882.

26 J. Tian, Q. Xue, X. Tang, Y. Chen, N. Li, Z. Hu, T. Shi, X. Wang, F. Huang, C. J. Brabec, H.-L. Yip and Y. Cao, *Adv. Mater.*, 2019, **31**, e1901152.

27 L. Zhang, M. Zhou, Z. Zhang, J. Yuan, B. Li, W. Wen and J. Tian, *J. Mater. Chem. A*, 2019, **7**, 22229-22234.

28 D. Yang, X. Li, W. Zhou, S. Zhang, C. Meng, Y. Wu, Y. Wang and H. Zeng, *Adv. Mater.*, 2019, **31**, 1900767.

29 H. Wang, Y. Wei, H. Li, X. Zhang, H. Qi, B. Tang, Y. Guo, L. Ye and H. Wang, *Adv. Mater. Interfaces*, 2021, **8**, 2100442.

30 G. Tang, P. You, Q. Tai, R. Wu and F. Yan, *Solar RRL*, 2018, **2**, 1800066.

31 Q. A. Akkerman, M. Gandini, F. Di Stasio, P. Rastogi, F. Palazon, G. Bertoni, J. M. Ball, M. Prato, A. Petrozza and L. Manna, *Nat. Energy*, 2016, **2**.

32 S. Oz, A. K. Jena, A. Kulkarni, K. Mouri, T. Yokoyama, I. Takei, F. Unlu, S. Mathur and T. Miyasaka, *ACS Energy Lett.*, 2020, **5**, 1292-1299.

33 L. N. Quan, F. P. García de Arquer, R. P. Sabatini and E. H. Sargent, *Adv. Mater.*, 2018, **30**, e1801996.

34 Y. Qian, Z. Zhang, W. Tian, L. Wen and L. Jiang, *Faraday Discuss.*, 2018, **210**, 101-111.

35 M. G. Goesten and R. Hoffmann, *J. Am. Chem. Soc.*, 2018, **140**, 12996-13010.

36 D. B. Straus, S. Guo, A. M. Abeykoon and R. J. Cava, *Adv. Mater.*, 2020, **32**, e2001069.

37 R. Chen, Y. Wang, S. Nie, H. Shen, Y. Hui, J. Peng, B. Wu, J. Yin, J. Li and N. Zheng, *J. Am. Chem. Soc.*, 2021, **143**, 10624-10632.

38 H. Y. Zhang, X. J. Song, H. Cheng, Y. L. Zeng, Y. Zhang, P. F. Li, W. Q. Liao and R. G. Xiong, *J. Am. Chem. Soc.*, 2020, **142**, 4604-4608.

39 R. Chen, Y. Hui, B. Wu, Y. Wang, X. Huang, Z. Xu, P. Ruan, W. Zhang, F. Cheng, W. Zhang, J. Yin, J. Li and N. Zheng, *J. Mater. Chem. A*, 2020, **8**, 9597-9606.

40 R. Chen, Y. Wu, Y. Wang, R. Xu, R. He, Y. Fan, X. Huang, J. Yin, B. Wu, J. Li and N. Zheng, *Adv. Funct. Mater.*, 2021, **31**, 2008760.

Supplementary Information

Supplementary information is not available with this version.

Figures

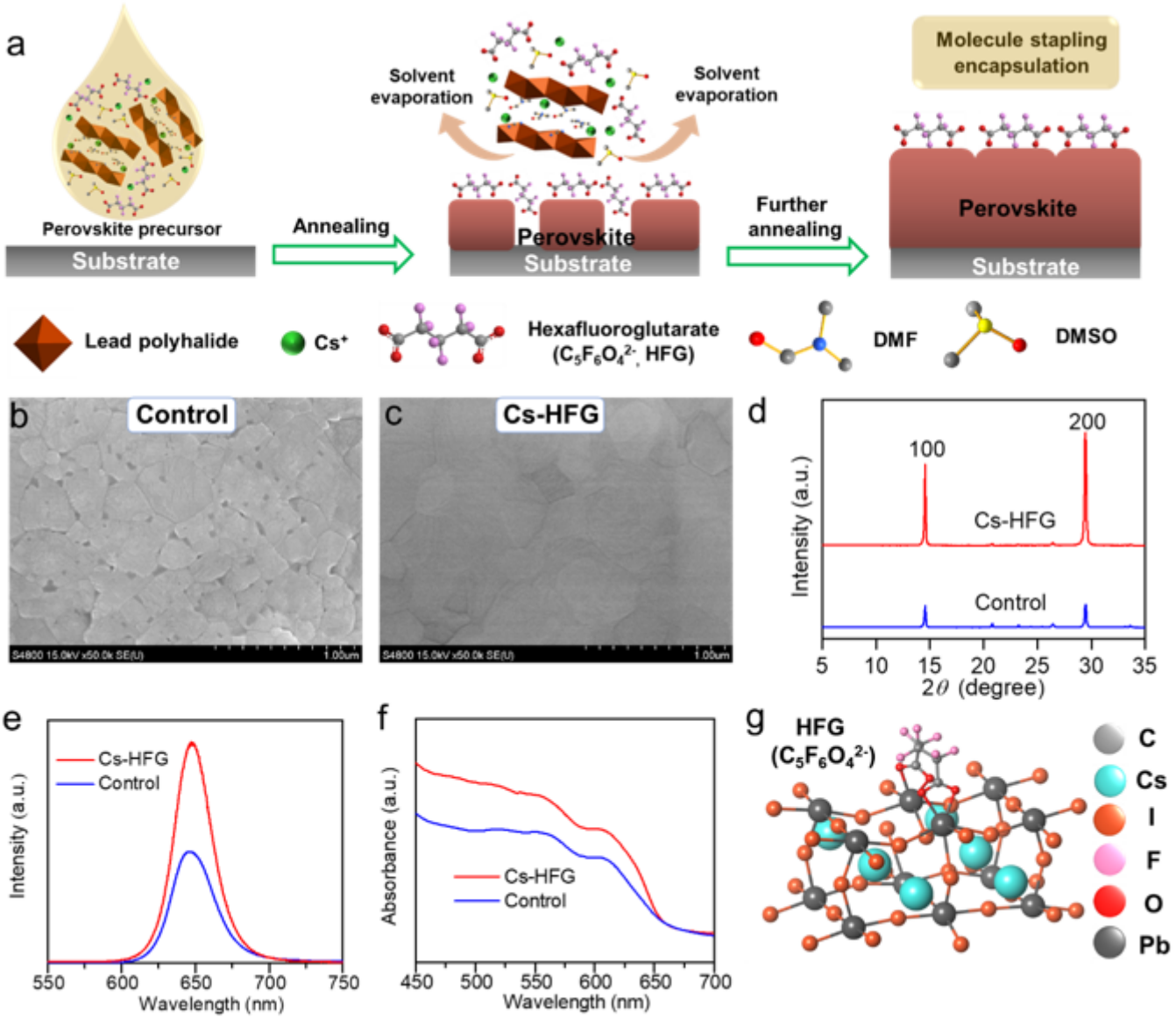

Figure 1

Morphology and structure of $CsPbI_2Br$ films by $C_5F_6O_4Cs_2$ stapling regulation. (a) Schematic illustration of the self-assembly of $C_5F_6O_4^{2-}$ on the surface and grain boundaries of perovskite films. (b, c) Surface morphology and (d) XRD patterns of control and Cs-HFG perovskite films. (e) PL and (f) UV–vis spectra of the control and Cs-HFG perovskite films. (g) Atomic structure of the optimized $CsPbI_3$ (001) surface with the $C_5F_6O_4^{2-}$ anion.

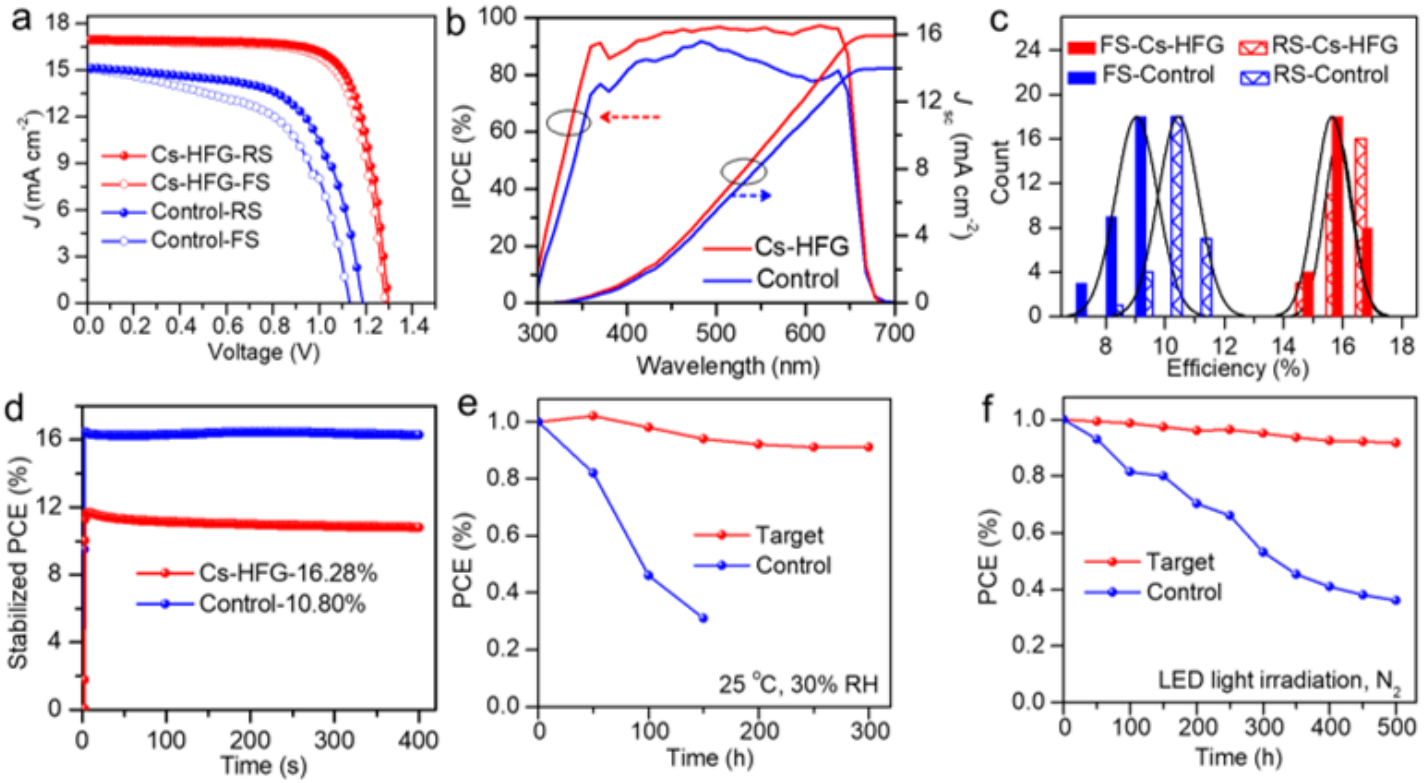

Figure 2

Characterization of $CsPbI_2Br$ PSCs without or with $C_5F_6O_4Cs_2$ stapling. (a) *J-V* curves of the champion devices based on control and Cs-HFG films (FS: forward scan, RS: reverse scan). (b) IPCE spectra and corresponding integrated short currents J_{sc} of the champion of control and Cs-HFG devices. (c) RS and FS efficiency distributions of 30 individual control and Cs-HFG devices. (d) Maximum power point tracking of control and Cs-HFG devices in 400 s under AM 1.5 G radiation. (e) Moisture stability of control and Cs-HFG devices at 25 °C and 30% RH. (f) Operation stability of control and Cs-HFG devices under LED light irradiation in a N_2 atmosphere.

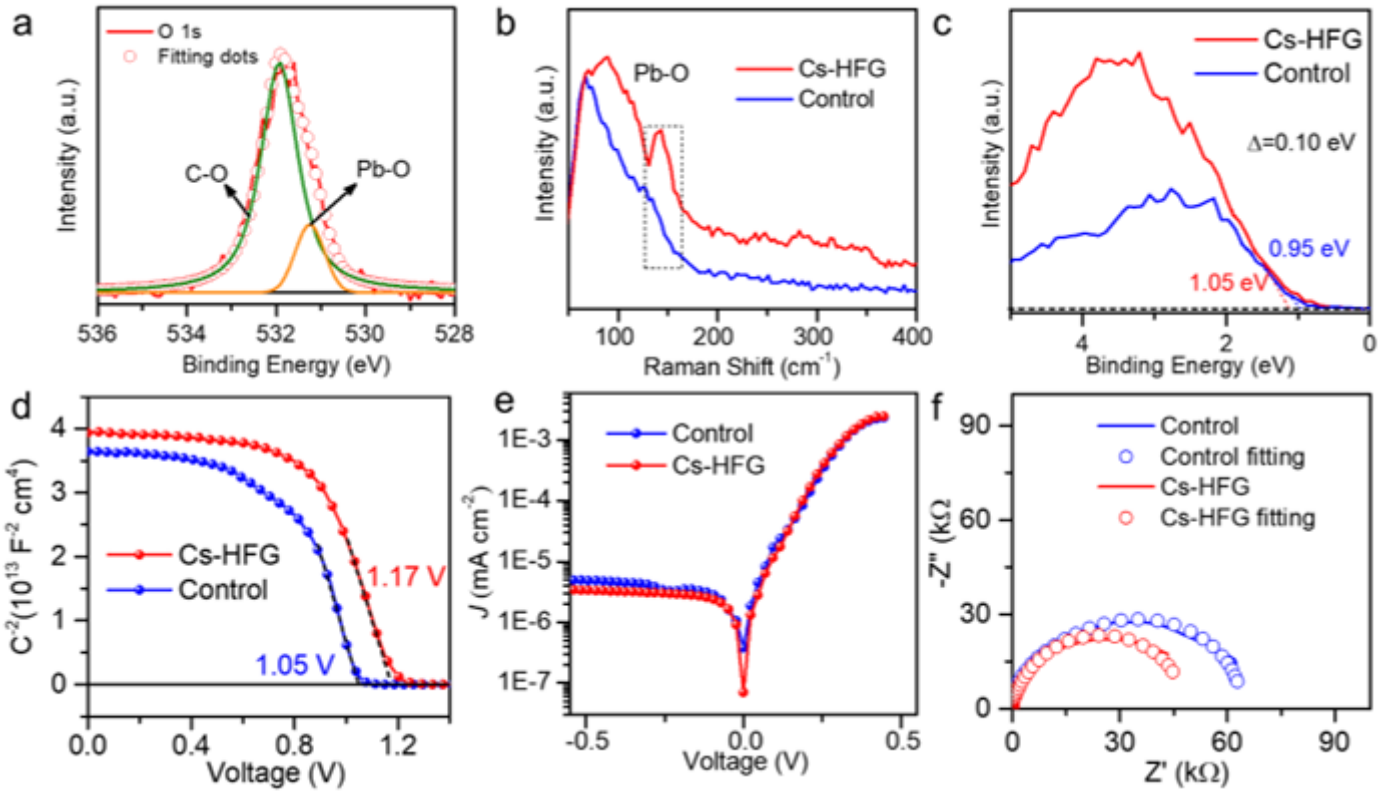

Figure 3

Surface chemical state of perovskite films and the electrical performance of PSCs. (a) O 1 s XPS spectra of the Cs-HFG perovskite films. (b) Raman spectra and (c) XPS valence band spectra of the control and Cs-HFG perovskite films. (d) Mott–Schottky analysis of the control and Cs-HFG devices at 1000 Hz. (e) Dark currents of device-based control and Cs-HFG perovskite films with a scan rate of 50 mV s^{-1} under dark conditions. (f) EIS characteristics of the champion PSCs with control and Cs-HFG films measured at 0 V bias under AM 1.5G conditions.

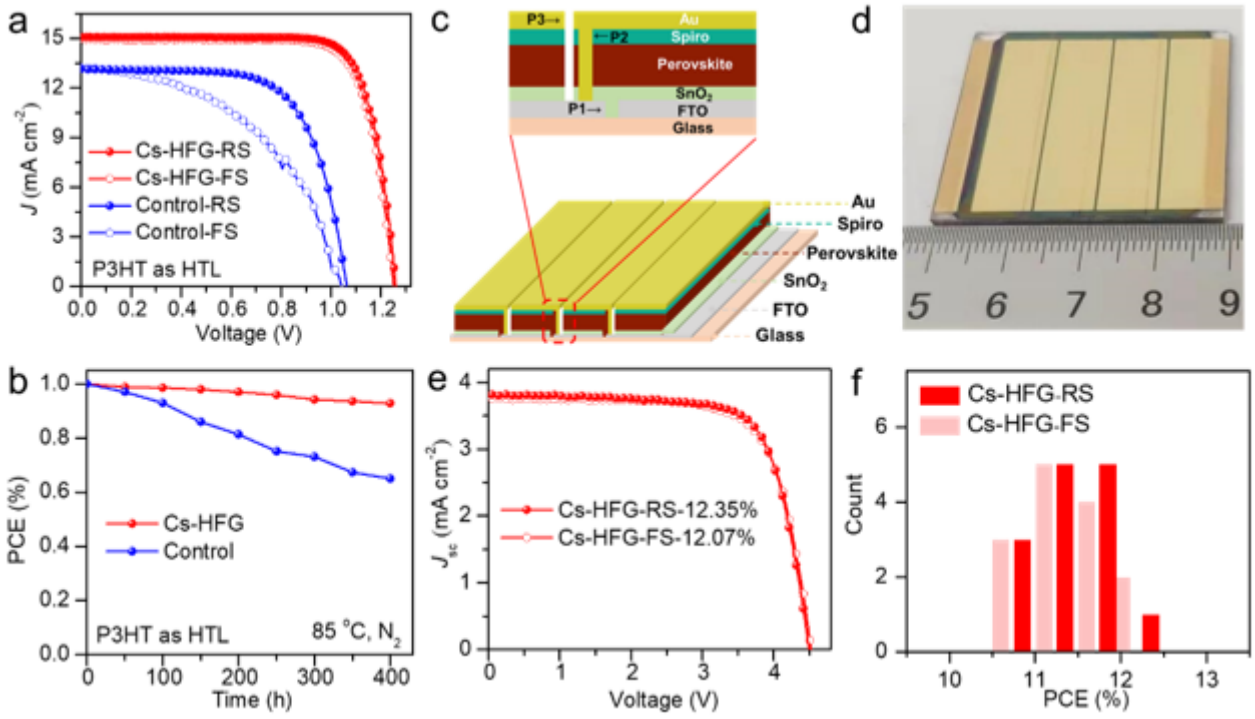

Figure 4

Thermal stability of small-area PSCs and large-scale fabrication of Cs-HFG-based PSC modules. (a) *J-V* curve of the champion cells based on control and Cs-HFG films with P3HT HTL. (b) Thermal stability of the devices measured at 85 °C in a N_2 atmosphere. (c) Schematic illustration and (d) photograph of a 16 cm^2 Cs-HFG-based module. (e) *J-V* curves of the champion Cs-HFG-based Cs-HFG-based module. (f) RS and FS efficiency distributions of 15 individual solar modules (16 cm^2) based on Cs-HFG films.